

# Ordered Electronic Reconstruction of the (11 $\bar{2}$ 0) ZnO Single Crystal

Narendra S. Parmar, Haena Yim, Lynn A. Boatner, Panithan Sriboriboon, Yunseok Kim, Kyung Song, Jung-Hae Choi, In Won Yeu, and Ji-Won Choi\*

Three-dimensional (3D) charge-written periodic peak and valley nanoarray surfaces are fabricated on a (11 $\bar{2}$ 0) ZnO single crystal grown via chemical vapor transport. Because the grown ZnO crystals exhibit uniform n-type conduction, 3D periodic nanoarray patterns are formed via oxygen annealing. These periodically decorated structures show that the peak arrays are conducting at the nanoampere level, whereas the valley arrays are less conductive. Energy dispersive spectroscopy indicates that the valley arrays are deficient in zinc by  $\approx 4$ –6 at%, and that the peak arrays are deficient in oxygen, respectively. Kelvin probe force microscopy reveals the presence of periodic wiggles featuring variations of  $\approx 70$ –140-meV between the peak and valley arrays. A significant decrease in the Fermi level of the valley region is observed ( $\approx 190$  meV), which corresponds to a high zinc vacancy doping density of  $2 \times 10^{18} \text{ cm}^{-3}$ . This result indicates the periodic generation of an extremely large electric field ( $\approx 11\,000 \text{ V cm}^{-1}$ ) in the vicinity of the peak–valley arrays. Computational analysis corroborates the experimentally observed generation of  $V_{\text{Zn}}$  and the preferential formation of surface protrusions on ZnO (11 $\bar{2}$ 0) rather than on (0001), based on surface effects, along with the generation of peak and valley features.

in optoelectronic devices<sup>[3]</sup> owing to its extremely slow deterioration, wide bandgap, and high excitonic stability. In particular, its large exciton binding energy ( $\approx 60$  meV)<sup>[4]</sup> is considerably higher than the thermal energy at room temperature, enabling its use in various photonic applications including light-emitting diodes, ultraviolet (UV) photovoltaics, and exciton–polariton lasing. Therefore, ZnO offers remarkable benefits for advanced photonic technologies. However, the key mechanisms of its high-performance photofunctionalities and full potential have not been comprehensively elucidated to date. Diffraction gratings, which are simple patterns constituting periodic arrays and spaces, are manufactured either conventionally using a ruling engine by burnishing grooves with a diamond stylus, or holographically<sup>[5]</sup> using interference fringes generated at the intersection of two coherent light beams. These techniques generally

require sophisticated and expensive equipment, complicated and precisely controlled fabrication processes, and extremely stable and clean fabrication environments. Therefore, a high-fidelity

## 1. Introduction

ZnO<sup>[1,2]</sup> is a remarkable material that exhibits various unusual electronic properties and is suitable for use

N. S. Parmar, H. Yim, J.-H. Choi, I. W. Yeu, J.-W. Choi  
Electronic Materials Research Center  
Korea Institute of Science and Technology  
Seoul 02792, Republic of Korea  
E-mail: jwchoi@kist.re.kr

L. A. Boatner  
Materials Science and Technology Division  
Oak Ridge National Laboratory  
Oak Ridge, TN 37831, USA

P. Sriboriboon, Y. Kim  
School of Advanced Materials Science and Engineering  
Sungkyunkwan University  
Suwon 16419, Republic of Korea

K. Song  
Materials Modeling and Characterization Department  
Korea Institute of Materials Science  
Changwon 51508, Republic of Korea

J.-W. Choi  
Division of Nano & Information Technology  
KIST School  
University of Science and Technology  
Daejeon 34113, Republic of Korea

 The ORCID identification number(s) for the author(s) of this article can be found under <https://doi.org/10.1002/aelm.202201336>

© 2023 The Authors. Advanced Electronic Materials published by Wiley-VCH GmbH. This is an open access article under the terms of the Creative Commons Attribution License, which permits use, distribution and reproduction in any medium, provided the original work is properly cited.

DOI: 10.1002/aelm.202201336

yet complicated replication technique involving resin casting of ruled and holographic master gratings onto a substrate was developed for the commercial production of gratings. The resulting replicas have been extensively used in diverse fields such as spectroscopy, metrology, and integrated optics. Other techniques involving lithography<sup>[6]</sup> and/or etching such as electron-beam lithography,<sup>[7]</sup> imprint lithography, and photolithography, have also been developed. Moreover, two-dimensional (2D) semiconductors have emerged as a new class of materials for nanophotonics owing to their strong exciton–photon interaction and their ability to be engineered and integrated into devices. ZnO also fits into this category.<sup>[8]</sup>

Defects in semiconductors play a key role in the manipulation of their electrical and optoelectronic properties. Intensive and long-term investigations of ZnO have been conducted in both academic and industrial settings to leverage its varied actual and potential applications in electronic and optoelectronic devices. Point defect engineering of ZnO has attracted particular attention because zinc vacancies have been theoretically and experimentally found to act as shallow acceptors, which play a crucial role in creating p–n junctions for the fabrication of blue/UV light-emitting diodes (LEDs). Thus, elucidation of the thermodynamics and kinetics of intrinsic point defects in ZnO is fundamentally and technologically important. Oxygen vacancies must be suppressed to minimize hole compensation. Additionally, zinc migration has been considered for interpreting the degradation of varistor devices that are believed to operate through the migration of intrinsic defects, most likely zinc interstitials. Additionally, insight into zinc defect diffusivities<sup>[9]</sup> is crucial for controlling the formation of undesirable and compensating defects, which can impede the synthesis of p-type ZnO. The most common strategy to create zinc vacancies involves either electron or laser irradiation, both of which are non-equilibrium thermodynamic processes that simultaneously generate compensating defects such as zinc interstitials, oxygen interstitials, and oxygen vacancies. It is relatively difficult to avoid and control the creation of these defects. Recently, Parmar et al.<sup>[10]</sup> reported the formation of isolated zinc vacancies at high concentrations ( $>10^{20}$  cm<sup>-3</sup>) at thermodynamic equilibrium. This approach can play a key role in obtaining p-type ZnO by controlling the formation of zinc vacancies, which act as shallow acceptors in the ZnO crystal. Zinc vacancies created by electron irradiation<sup>[11]</sup> and laser radiation<sup>[12]</sup> have been extensively examined to evaluate the self-diffusion of zinc in ZnO. However, the experimental data obtained to date exhibit considerable variations, which hinders their interpretation. Therefore, a joint theoretical and experimental study can provide valuable insights into the various atomistic migration processes and consequently assist in quantifying their respective contributions, while a series of structural transformations and reconstructions on a semiconductor can be useful for various technological applications, where electrical manipulations are possible.<sup>[13,14]</sup>

In this study, electrically decorated periodic three-dimensional (3D) peak and valley nanosurface structures are fabricated on a (11 $\bar{2}$ 0) ZnO single crystal grown via chemical vapor transport (CVT).<sup>[15]</sup> Thereby, we aim to facilitate the synthesis of 3D/2D mixed-dimensional nano-periodic arrays of (11 $\bar{2}$ 0) ZnO with selective doping, thereby promoting optoelectronic and other technological applications of ZnO.

## 2. Results

Nanoarrays with peak-and-valley-decorated periodic structures were observed using atomic force microscopy (AFM). Peak-to-valley heights of  $\approx 30$ – $40$  nm, peak-to-peak distances of  $\approx 320$  nm, and peak widths of  $\approx 200$  nm were obtained. **Figure 1a** shows a schematic of the AFM measurements, while a plot of the variation in the height ( $z$ ) of the topography is shown in **Figure 1c**. In addition, a plot of the variation in  $z$  direction (**Figure 1d**) on a straight line indicated by the five points is outlined in **Figure 1c**.

In addition, conductive atomic force microscopy (CAFM) measurements were performed. The current profile of a line including seven points (across the peaks and valleys) in the CAFM image displayed in **Figure 2a** is shown in **Figure 2b**, while the average currents in the peak and valley regions are depicted in **Figure 2c**. The average current in the peak region was  $\approx 1$  nA, whereas the valley region did not exhibit conduction (only noise current). The current profiles of the peak and valley regions highlighted in the CAFM image in **Figure 2d** are presented in **Figure 2e**. The current corresponding to the peak-featuring line was  $\approx 1$  nA, whereas the valley-featuring line did not exhibit conduction (only noise current).

Figures S1 and S2 (Supporting Information) shows the CAFM images of two regions of pristine ZnO samples. The topographical images did not reveal any specific periodic array patterns, while the conduction was almost uniform without any dependence on the tip bias (+ 4.0 V).

Lateral force microscopy (LFM) was performed, which can effectively illustrate variations in the surface friction arising from inhomogeneities on the material surfaces. The friction force on the surface strongly depends on the carrier concentration of the material surface. **Figure 3a** shows the variation in the lateral force signal ( $z$ -direction), while **Figure 3b** displays a plot of the lateral force signal in the peak and valley regions corresponding to the yellow and white lines that are shown in **Figure 3a**. The lateral force signals of the peaks are higher than those of the valleys. Together with the CAFM results, the LFM results suggest that the valley regions are charge-depleted.

Contact potential difference (CPD) profiles across the surface were acquired, and the corresponding potentials were measured, as shown in **Figure 3c**. Moreover, the differences in the work functions of the tip ( $\varphi_{\text{Tip}}$ ) and sample surface ( $\varphi_{\text{Sample}}$ ) generate  $V_{\text{CPD}}$  upon electrical contact, which is defined as

$$V_{\text{CPD}} = \frac{\varphi_{\text{Tip}} - \varphi_{\text{Sample}}}{q \text{ (the electronic charge)}} \quad (1)$$

**Figure 3c** illustrates the variation in the surface potentials of the peak and valley structures of the ZnO crystal obtained by Kelvin probe force microscopy (KPFM) in a dark chamber, whereas **Figure 3d** shows the corresponding topographical image. The potential depth profiles shown in **Figure 3c** exhibit two important qualitative features: the periodic distribution of the potential drop ( $\approx 70$ – $140$  mV) throughout the selected crystal region between the peak and valley structures. Valley was determined to be zinc deficient, which has a lower contact potential than the peak. The variation in the potential indicates the nature of the charge due to the variations in zinc vacancies. The potential drop

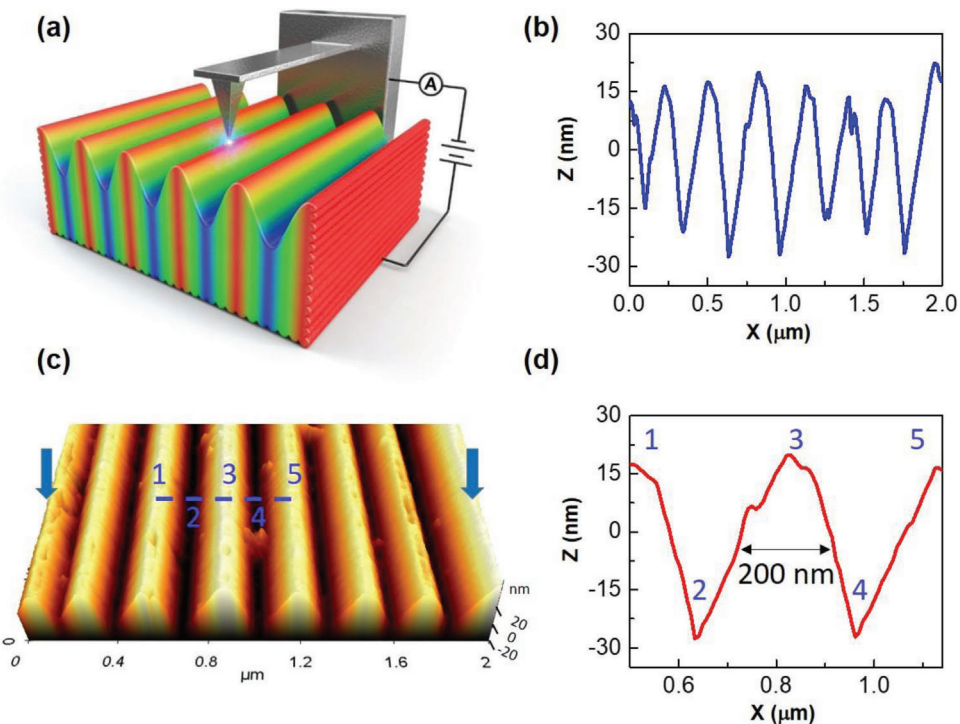


**Figure 1.** AFM analysis. a) Schematic setup. b) Variation in z-direction of the periodic peak–valley regions. c) Topographical image of the crystal showing periodic peak–valley nanoarrays. d) Variations in the peak-to-peak distance, peak width, and peak height of the five points shown in (c).

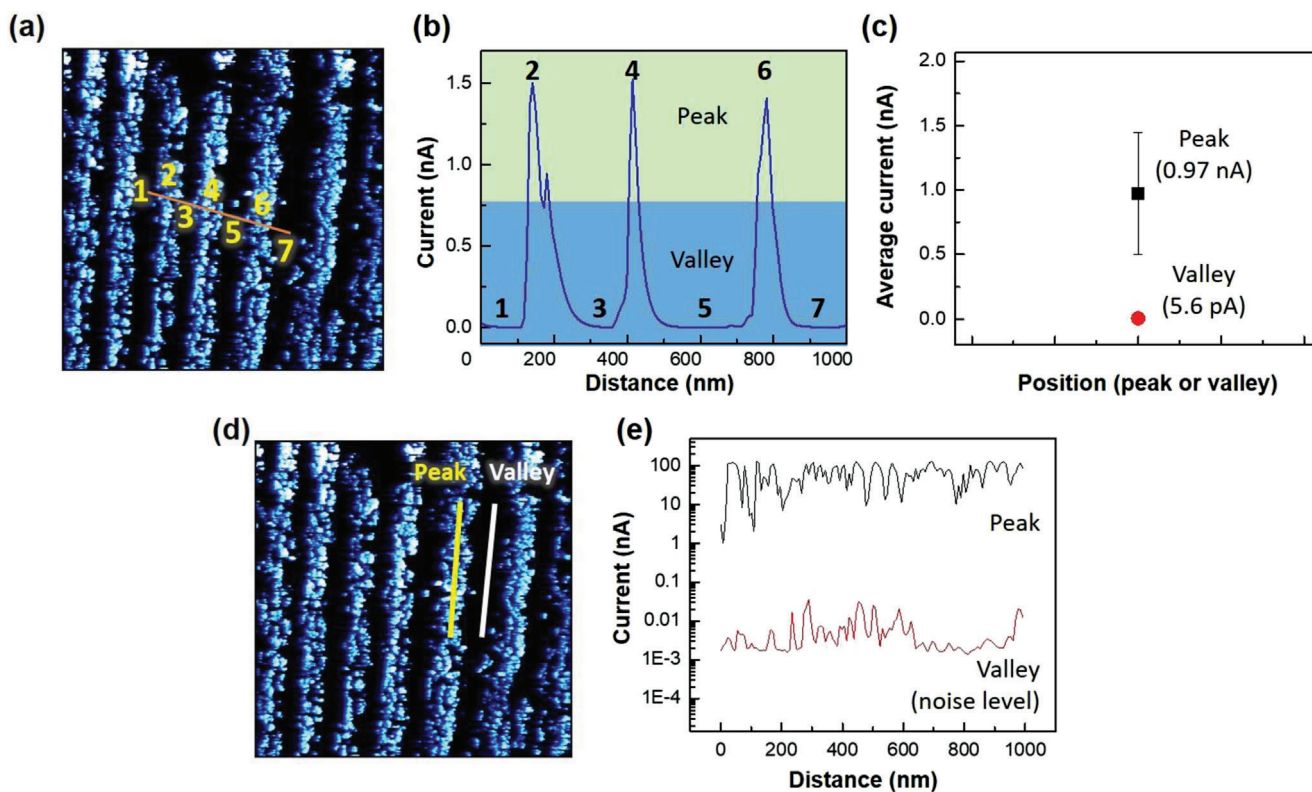


**Figure 2.** CAFM images acquired using tip biases of a) + 0.3 V and d) + 2 V. b) Current profile corresponding to the seven points shown in (a). c) Average peak and valley currents. e) Profiles of the peak and valley regions highlighted in (d).

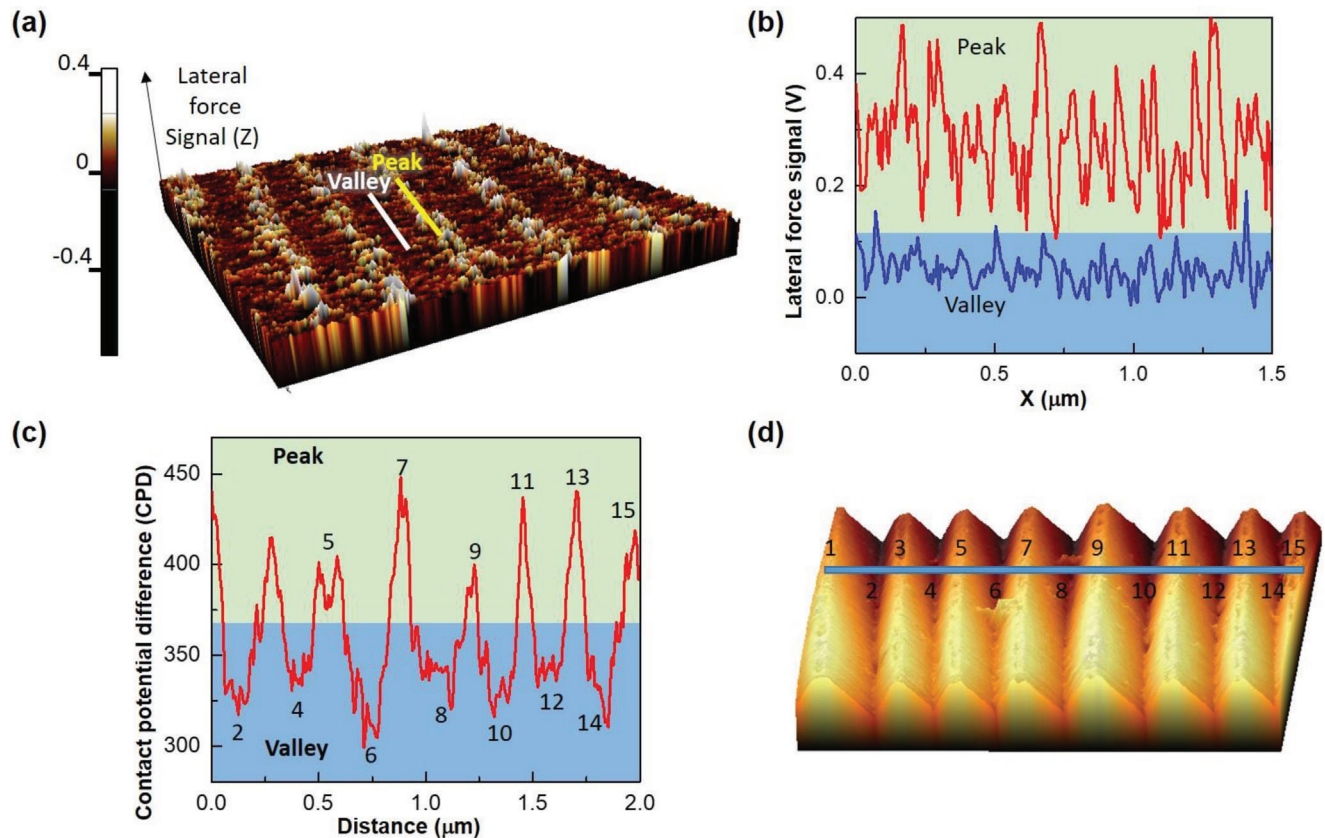


**Figure 3.** LFM analysis. a) Variation in the lateral force signal (z-direction), and b) a plot of the lateral force signals in the peak and valley regions corresponding to the lines shown in (a). KPFM measurements indicating the lack of an equipotential surface. c) Variation in the potential with the periodic peak and valley regions. d) Topographical micrograph featuring a line with fifteen points corresponding to various peaks and valleys.

generated inside the ZnO crystal, including the peak and valley structures, was calculated as is described in the next section.

### 2.1. Calculation of the Gradient Electric Field

$$\Delta V = -E \Delta x \text{ (scalar version is assumed)} \quad (2)$$

Therefore,

$$\text{grad } E = \frac{\Delta V}{\Delta x} \quad (3)$$

The KPFM measurement of point #4 in Figure 3c provides the following values.

$$\Delta V \approx 140 \text{ mV and } \Delta x \approx 50 \text{ nm} \quad (4)$$

Therefore,

$$\begin{aligned} \text{grad } E &= \frac{\Delta V}{\Delta x} = \frac{140 \times 10^{-3} \text{ V}}{50 \times 10^{-7} \text{ cm}} \\ &= 5.6 \times 10^4 \text{ V cm}^{-1} \approx 56 \text{ kV cm}^{-1} \end{aligned} \quad (5)$$

### 2.2. Calculation of the Charge Carrier Density

The charge carrier concentration  $n_o$  in a semiconductor under an imposed electric field is given by

$$n_o = \frac{\epsilon \epsilon_o E_m}{qt} \quad (6)$$

where  $\epsilon$  is the dielectric constant,  $E_m$  is the maximum electric field,  $q$  is the electronic charge, and  $t$  is the valley width. Therefore,  $n_o$  can be estimated using Equation (3), as follows:

$$n_o = \frac{8.5 \times 8.85 \times 10^{-12} \times 1.12 \times 10^6}{1.6 \times 10^{-19} \times 1.25 \times 10^{-7}} = 2.1 \times 10^{16} \text{ cm}^{-3} \quad (7)$$

### 2.3. Calculation of Fermi Level

The Fermi level of a semiconductor can be calculated according to:

$$|E_F| = \hbar v_f (\pi |n_o|)^{1/2} \quad (8)$$

where  $v_f$  is the Fermi velocity,  $\hbar$  is the reduced Planck's constant, and  $n_o$  is the charge-carrier density. Assuming

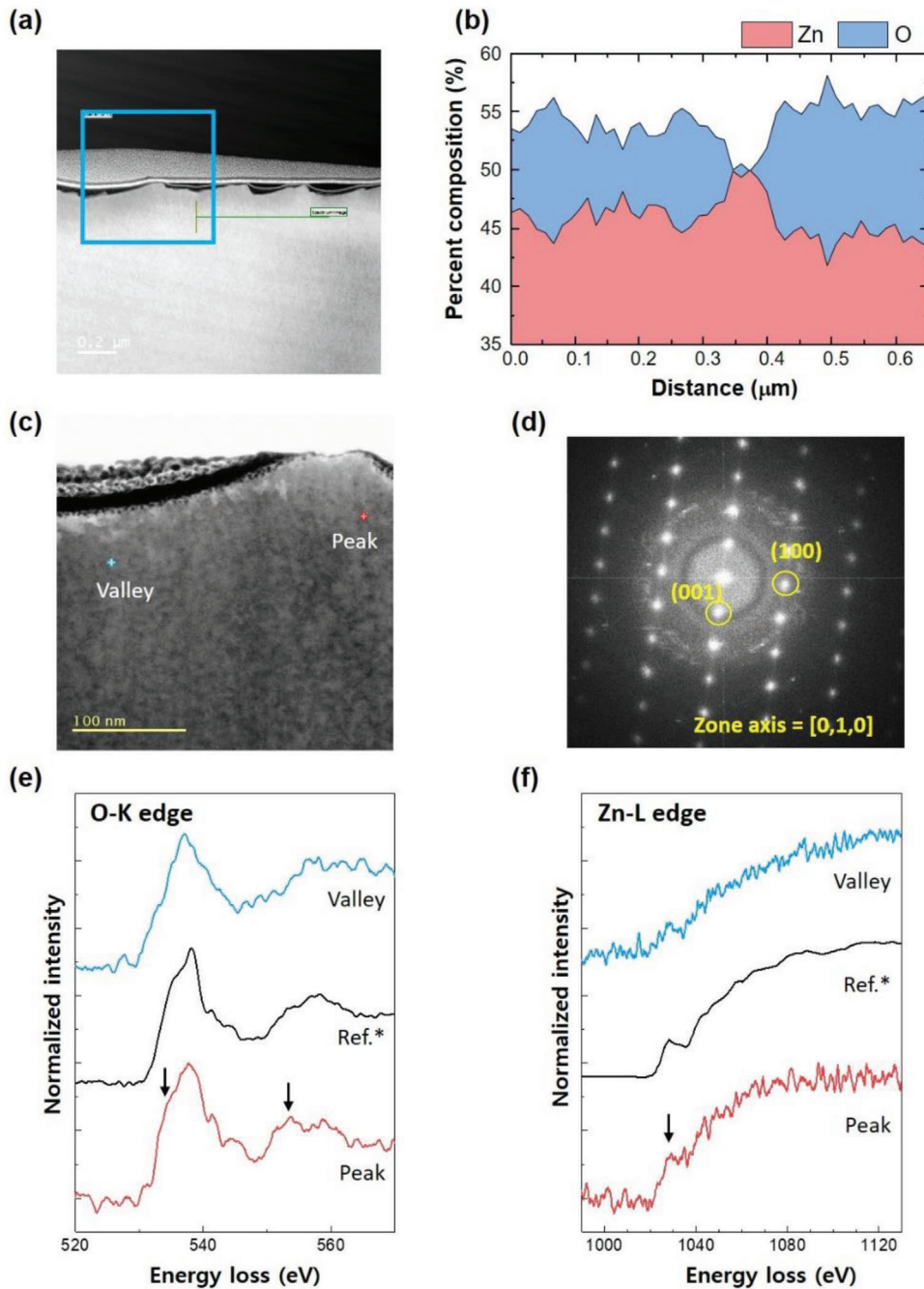


**Figure 4.** a) STEM micrograph of the selected region containing two valleys and one peak. b) EDS profiles indicating the oxygen and zinc deficiency of the peak and valley regions, respectively. c) HRSTEM image of the valley and peak regions. d) Corresponding single-crystal electron diffraction pattern. e) O-K edge ELNES measurement data of the valley and peak points and the reference ZnO powder. f) ELNES measurement data showing the absence of the Zn-L3 edge in the valley region because of its zinc deficiency, compared to those of the peak and reference ZnO powder. Vertical arrows indicate the relevant identified peaks in the O-K and Zn-L3 edge spectra.

$v_f = 1.1 \times 10^6 \text{ ms}^{-1}$ ,  $|E_F|$  can be calculated accordingly:

$$|E_F| = 6.6 \times 10^{-16} \times 1.1 \times 10^6 (6.59 \times 10^{16})^{1/2} \approx 190 \text{ meV} \quad (9)$$

Electron diffraction spectroscopy (EDS) analysis was carried out for qualitative analysis of the deficiencies of zinc and oxygen. The EDS profiles suggested that the valley array was  $\approx 4\text{--}6$  at%

deficient in zinc, and that the peak array was deficient in oxygen, as shown in **Figure 4**. These results confirm that the valley part represents p-type zinc deficiencies, while the peak part represents n-type deficiencies.

Figure 4c shows a high-resolution scanning transmission electron microscopy (HRSTEM) cross-sectional image of ZnO containing peak and valley structures. Figure 4d presents the

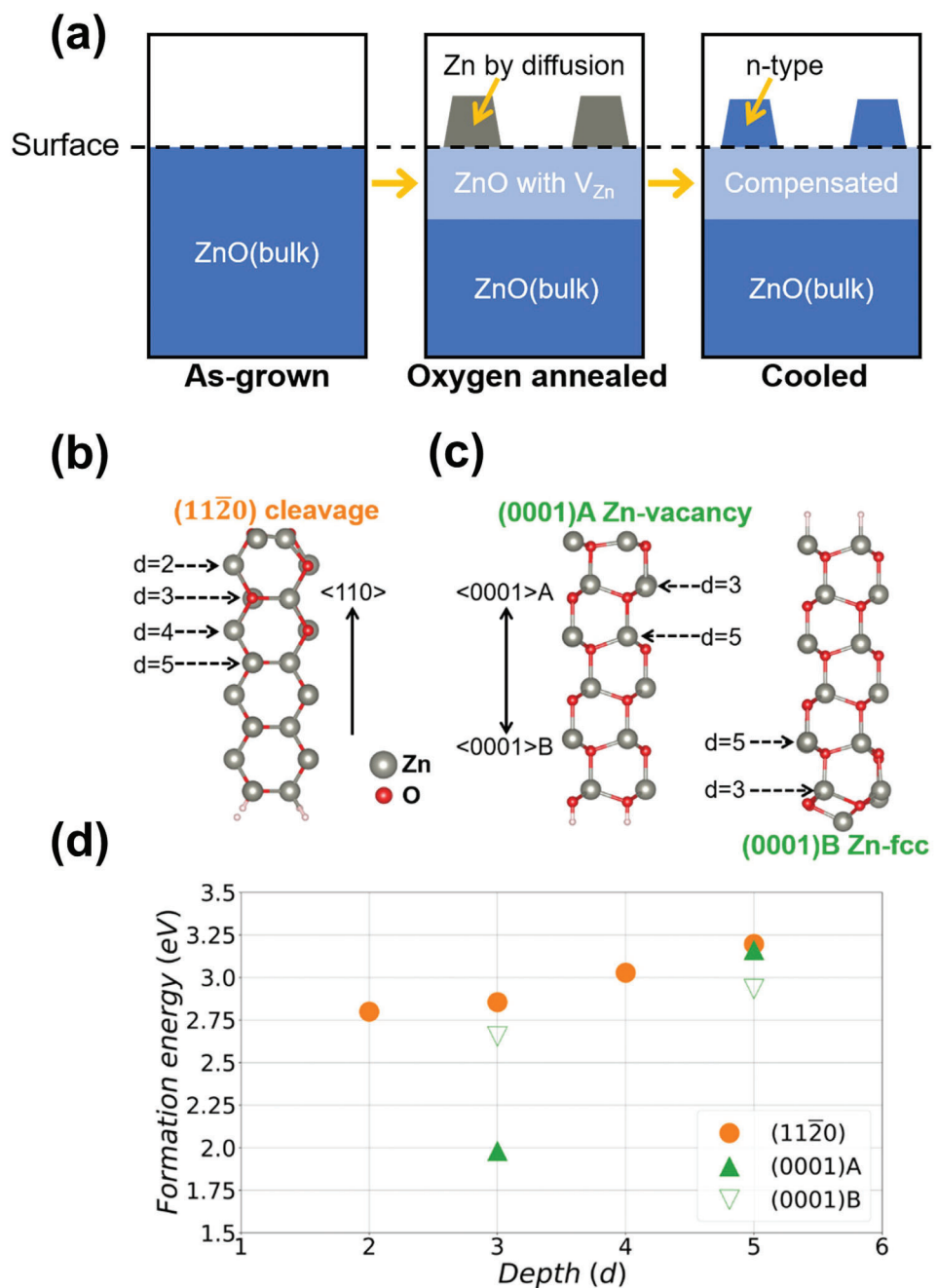


**Figure 5.** Effects of the surface reconstruction on the  $V_{Zn}$  formation energy. Illustration of the changes in the zinc vacancy ( $V_{Zn}$ ) concentration and surface morphology by the post-growth processes involving oxygen-annealing at 1100–1200 °C and  $\approx 1500$  Torr followed by a cooling process. The ZnO regions with low and high concentrations of  $V_{Zn}$  are represented by dark and light blue regions, respectively. Side views of the a)  $(11\bar{2}0)$ , b)  $(0001)A$ , and  $(0001)B$  ZnO reconstructions. The  $n$ th layer ( $d = n$ ) from the topmost surface, which permits  $V_{Zn}$  formation, is numbered accordingly. c) Calculated  $V_{Zn}$  formation energy as a function of the depth  $d$  at 1400 K and 1500 Torr.

corresponding single-crystal electron diffraction pattern. The HRSTEM images for the regions of peak and valley area are presented in Figure S3 (Supporting Information), and all areas indicate its single crystal nature. However, the difference is that the local lattice defects is not observed in peak area and the local lattice distortion induced by defects in valley area. Additionally, Figure 4e displays the energy loss near-edge structure (ELNES)

profiles of the O-K edge of the ZnO peak, valley, and powder, while Figure 4f shows the corresponding Zn-L edge profiles. The clear dissimilarity between the two sets of spectra proves that the valley and peak regions of ZnO agree with the EDS results shown in Figure 5b. Small differences were observed in the O-K/Zn-L edge spectra of the peak regions, as indicated by the arrows. These differences presumably indicate differences in the zinc

environment. Similar features in the O-K edge spectra of ZnO were interpreted by Sato et al.<sup>[16]</sup> to be due to zinc vacancies, based on a comparison with theoretical calculations. The sharp features of the Zn-L3 edge were clearly missing in the valley region, corroborating its zinc-deficient nature, as shown in Figure 4b. The ELNES data further confirmed the zinc-deficient nature of the valley region compared to that of the peak region.

#### 2.4. Computational Analysis

The schematic image in Figure 5 summarizes the experimental findings regarding the changes in the zinc vacancy ( $V_{\text{Zn}}$ ) concentration and its effects on the surface morphology during the oxygen annealing and cooling processes. Based on a previous study, high concentrations of  $V_{\text{Zn}}$  ( $>10^{20} \text{ cm}^{-3}$ ) were formed in the region that is 100–150 nm near the surface during post-processing (adding ref. [14]). In terms of the electrical properties, the native n-type conductivity of ZnO was compensated by the high concentrations of  $V_{\text{Zn}}$  near the surface (corresponding to the valley positions in the experiments) owing to the electron-accepting nature of  $V_{\text{Zn}}$ .<sup>[17]</sup> In contrast, the ZnO protrusions (corresponding to the peak positions) exhibited n-type conductivity. Janotti and Van de Walle<sup>[17]</sup> thoroughly investigated the formation energy of native point defects in ZnO using density functional theory (DFT) calculations, and found that the  $V_{\text{Zn}}$  formation energy decreased under oxygen-rich conditions. This is the fundamental reason for  $V_{\text{Zn}}$  formation on the surface region, as the environmental conditions around ZnO transform into an oxygen-rich atmosphere during oxygen annealing, thereby leading to a driving force to achieve an equilibrium concentration with a higher  $V_{\text{Zn}}$  content by diffusing out Zn atoms to the surface.

#### 2.5. Surface Effects

The surface structure is known to considerably affect the solubility of point defects.<sup>[18]</sup> Therefore, different surface structures were investigated to determine the possible effects on the  $V_{\text{Zn}}$  formation. The (11 $\bar{2}$ 0) and (0001) surfaces are representative of nonpolar and polar surfaces of wurtzite (WZ) ZnO without an inversion center, respectively. The polar (0001) surface, also known as the basal or c-plane, can be further divided into the inequivalent (0001)A and (0001)B.<sup>[19]</sup> Moreover, the nonpolar (11 $\bar{2}$ 0) surface in the Miller–Bravais indices, also known as the a-plane, is commensurate with the zinc blende (ZB) (110) and (112) surfaces in the Miller indices.<sup>[20,21]</sup> The surface energy of this nonpolar surface can be readily calculated using conventional slab methods (steps 1 and 2 in Sections S2-2, Supporting Information). However, estimation of the individual surface energies of (0001)A and (0001)B using DFT calculations is difficult because of the simultaneous formation of zinc-terminated (0001)A and oxygen-terminated (0001)B surfaces on the top and bottom surfaces of the (0001) slab, respectively. Therefore, a heterojunction model<sup>[22]</sup> was adopted to address the inaccessibility of the WZ polar surface energy. The calculation method is described in detail in Sections S2-2 (Supporting Information). The obtained surface energies of the ZnO (11 $\bar{2}$ 0), (0001)A, and (0001)B reconstructions are shown in Figure S6c–e (Supporting Information).

As explained in Sections S2–S4 (Supporting Information), the effects of high temperature and pressure on the surface structure transitions were also considered using ab-initio atomistic thermodynamics, which have been shown to bridge the gap in analyses performed with respect to temperature and pressure between the standard surface characterizations conducted at low temperatures and pressures (even 0 K in DFT calculations) and realistic surface reactions performed at high temperatures and pressures, such as surface transitions,<sup>[23,24]</sup> catalysis,<sup>[25]</sup> and growth behavior.<sup>[26–28]</sup> Under experimentally relevant conditions of  $\approx 1400$  K and 1500 Torr, the stable surface structures of (11 $\bar{2}$ 0), (0001)A, and (0001)B WZ-ZnO were predicted to be cleavage ( $1 \times 1$ ), zinc-vacancy ( $2 \times 2$ ), and zinc-fcc ( $2 \times 2$ ), respectively. The corresponding surface energies were estimated to be  $\approx 56$ , 80, and 80 meV  $\text{\AA}^{-2}$ , respectively (Sections S2–S4 and Figure S6, Supporting Information). Side views of the stable surface structures are shown in Figure 5b,c. The possible influence of these different surface structures on  $V_{\text{Zn}}$  formation was investigated by calculating the  $V_{\text{Zn}}$  formation energy as a function of its formation depth from the topmost surface layer:

$$\Delta E_{V_{\text{Zn}}}^d = E_{V_{\text{Zn}}}^d + (\mu_{\text{ZnO}(\text{bulk})} - \mu_{\text{O}(\text{O}_2)}) - E_{\text{surf}} \quad (10)$$

where  $\Delta E_{V_{\text{Zn}}}^d$  is the  $V_{\text{Zn}}$  formation energy at a certain depth  $d$ .  $E_{V_{\text{Zn}}}^d$  and  $E_{\text{surf}}$  are the energies of the surface slabs with and without  $V_{\text{Zn}}$ , and  $(\mu_{\text{ZnO}(\text{bulk})} - \mu_{\text{O}(\text{O}_2)})$  is the equilibrium chemical potential of zinc in ZnO. The chemical potential of bulk ZnO ( $\mu_{\text{ZnO}(\text{bulk})}$ ) was obtained using the Phonopy<sup>[29]</sup> program, and that of an oxygen molecule ( $\mu_{\text{O}(\text{O}_2)}$ ) was calculated using the method described in Sections S2–S4 (Supporting Information). Figure 5d shows the obtained  $\Delta E_{V_{\text{Zn}}}^d$  for each stable surface reconstruction achieved under conditions of 1400 K and 1500 Torr. For all of the relevant surfaces of (11 $\bar{2}$ 0) cleavage, (0001)A zinc-vacancy, and (0001)B zinc-fcc, the  $V_{\text{Zn}}$  formation energies were smaller near the surface but converged to  $\approx 3$  eV, which possibly corresponds to the  $V_{\text{Zn}}$  formation energy in bulk because of the increasing depth of  $V_{\text{Zn}}$ . In addition,  $V_{\text{Zn}}$  formation was considerably more likely to occur in (0001)A than in (11 $\bar{2}$ 0) because of the difference in their formation energies of 0.8 eV. Therefore, although the surface energy of (11 $\bar{2}$ 0) was the lowest, the formation of protrusions with the (0001) side facet on the (11 $\bar{2}$ 0) plane could help to achieve an enhanced equilibrium concentration of  $V_{\text{Zn}}$  during oxygen annealing. This explains the formation of peak and valley 3D nanoarray periodic patterns after the oxygen annealing procedure.

### 3. Discussion

The formation of the periodic peak and valley regions has not yet been comprehensively elucidated. The LFM analysis presented herein suggests that the peaks featured higher friction than that of the valley region, leading to stronger signals, and the zinc-deficient valleys yielded weaker signals. The valley region is rich in zinc vacancies that are responsible for generating holes and the resulting compensation of n-type conduction and the consequent insulating behavior, as indicated by the CFAM noise-level current signal. The O-deficient peak region exhibits n-type conduction with a nanoampere-scale current because oxygen

vacancies are responsible for n-type conduction in the ZnO crystals. The formation of peak protrusions despite the minimal surface energy of nonpolar (11 $\bar{2}$ 0) may be related to anisotropic chemistry because of the change in environmental conditions into an oxygen-rich atmosphere. Numerous zinc atoms presumably diffuse out to the surface to achieve a different equilibrium  $V_{Zn}$  concentration, and the introduction of other surface facets with protrusions can accelerate  $V_{Zn}$  formation. There are unresolved issues related to the potential formation of 3D nanoarray periodic patterns upon the transformation of the nonpolar (11 $\bar{2}$ 0) plane into other surfaces such as polar (0001). Furthermore, the possible role of kinetic effects in addition to anisotropic thermodynamics (differences in surface energy and  $V_{Zn}$  formation energy among crystallographically distinct surfaces) will be considered in our future investigations.

#### 4. Conclusion

Serial and parallel charge writing on a (11 $\bar{2}$ 0) ZnO single-crystal surface was realized on 3D periodic peak–valley nanoarray structures. The peak and valley arrays were found to be conducting at the nanoampere level and less conductive, respectively. Computational analysis validated the experimentally observed  $V_{Zn}$  generation and surface protrusions based on surface effects. These results can be beneficial for the fabrication of homojunction p–n devices in UV/blue LEDs.

#### 5. Experimental Section

**Methods:** CVT-grown ZnO crystals were placed in high-purity quartz ampoules (Heraeus) that were evacuated using roughing and turbomolecular pumps and subsequently baked at  $\approx 150$  °C overnight to remove residual water vapor. The vacuum pressure was varied from  $\approx 10^{-7}$  Torr prior to backfilling with ultra-high-purity oxygen to  $\approx 300$  Torr. The ampoules were sealed using an oxyhydrogen torch and placed in a tube furnace. Annealing was performed at 1100 °C or 1200 °C for 24 h. The ampoules remained in the furnace during cooling. Below a temperature of 1100 °C, the nanostructure cannot be formed because of insufficient temperature for the formation of peak and valley 3D nanoarray periodic patterns. Also, if the temperature is greater than 1200 °C, the nanostructure collapses because of excessive energy for the surface structure transitions. The zinc-vacancy-rich valley arrays and peak arrays were found to be less conductive and conducting, respectively. The periodically decorated peak–valley structures were validated by AFM. Conductive AFM and IV spectroscopy were performed to obtain current–voltage ( $I$ – $V$ ) profiles of the peak and valley regions. The differences in the voltage profiles of the peak and valley regions were evaluated using KPFM. LFM was employed to obtain insights into the frictional force profiles. DFT calculations were performed to corroborate the zinc-vacancy-induced surface reconstruction.

**Atomic Force Microscopy (AFM):** Topographical AFM images (Park Systems, Inc.) of oxygen-annealed ZnO crystals were collected in tapping mode.

**Conductive Atomic Force Microscopy (CAFM):** CAFM measurements were performed using a commercial atomic force microscope (NX10, Park Systems) with an external current amplifier

(DLPCA-200, FEMTO) using Pt/Ir-coated and Cr/Pt-coated conductive tips (Multi75E-G, Budget Sensor). The CAFM measurements were obtained by applying a voltage to the AFM tip with a contact force of 50 nN (set-point). Figure S1a,d (Supporting Information) shows CAFM images acquired using tip biases of a) + 0.3 V and d) + 2 V, respectively. Periodic variations in the current profiles were observed, with peak and valley currents in the nA and pA (noise-level) ranges, respectively (Figure S1b,c, Supporting Information) corresponding to the red and green lines in Figure S1a (Supporting Information). The results presented in Figure S1e,f (Supporting Information) correspond to the red and green lines, respectively, shown in Figure S1d (Supporting Information).

**Kelvin Probe Force Microscopy (KPFM):** KPFM is an established technique for characterizing nanoscale electronic/electrical properties of metal/semiconductor surfaces and devices. The electrostatic interactions between the conductive tip and the material surface during KPFM measurements enable surface mapping of the local electric charge distribution and the corresponding potential. Moreover, KPFM has recently been employed to acquire the surface potential depth profiles of different surface crystals, including p–n-type conduction layers. The surface potential depends on the number of charge carriers trapped on the cross-sectional surface and in the near-surface region. The interfaces between the different layers in the ZnO crystal were identified using cross-sectional imaging.

**Scanning Tunneling Electron Microscopy (STEM):** High-resolution transmission electron microscopy (HRTEM) analysis was performed using an FEI Titan 80–300 microscope operated at 300 keV with a resolution higher than 1 Å. Images were recorded using a 4k  $\times$  4k charge-coupled device (CCD) camera (Gatan, Oneview1095).

**Energy Dispersive Spectroscopy (EDS):** EDS profiles were acquired using a Cs-corrected microscope operated at 300 kV and equipped with a Gatan Quantum 966 spectrometer.

**Energy Loss Near-Edge Structure (ELNES) Analysis:** ZnO samples for the HRSTEM-based ELNES experiments were subsequently prepared to further examine their chemical compositions. Similar samples containing ZnO powder (99.9995% purity) were also prepared for comparison.

#### Supporting Information

Supporting Information is available from the Wiley Online Library or from the author.

#### Acknowledgements

N.S.P. and H.Y. equally contributed to this work. This research was supported by the National Research Foundation of Korea (NRF) Brain Pool Grant (No. 2019H1D3A2A02102942), the Korea Institute of Science and Technology Future Resource Program (2E32491), and an NRF grant provided by the Korean government (2021R1A2C2010695) and (2020R1A2C2003931).

#### Conflict of Interest

The authors declare no conflict of interest.

## Data Availability Statement

The data that support the findings of this study are available from the corresponding author upon reasonable request.

## Keywords

chemical vapor transport, nanoarray patterns, selective doping, the peak-valley arrays, ZnO

Received: January 1, 2023

Revised: March 28, 2023

Published online:

- 
- [1] A. Tsukazaki, A. Ohtomo, T. Onuma, M. Ohtani, T. Makino, M. Sumiya, K. Ohtani, S. F. Chichibu, S. Fuke, Y. Segawa, H. Ohno, *Nat. Mater.* **2005**, 4, 42.
- [2] A. Janotti, C. G. Van de Walle, *Nat. Mater.* **2007**, 6, 44.
- [3] M. V. Kelso, N. K. Mahenderkar, Q. Z. Chen, J. Z. Tubbesing, J. A. Switzer, *Science* **2019**, 364, 166.
- [4] C. G. Van De Walle, *Phys. Rev. Lett.* **2000**, 85, 1012.
- [5] A. C. Diebold, *Science* **2005**, 310, 61.
- [6] D. Pires, J. L. Hedrick, A. De Silva, A. J. F., B. Gotsmann, H. Wolf, M. Despont, U. Duerig, A. W. Knoll, *Science* **2010**, 328, 732.
- [7] A. Hatzor, P. S. Weiss, *Science* **2001**, 291, 1019.
- [8] E. Y. Paik, L. Zhang, G. W. Burg, R. Gogna, E. Tutuc, H. Deng, *Nature* **2019**, 576, 80.
- [9] N. S. Parmar, L. A. Boatner, K. G. Lynn, J. W. Choi, *Sci. Rep.* **2018**, 8, 13446.
- [10] N. S. Parmar, J. W. Choi, L. A. Boatner, M. D. McCluskey, K. G. Lynn, *J. Alloys Compd.* **2017**, 729, 1031.
- [11] F. Tuomisto, K. Saarinen, D. C. Look, *Phys. Status. Solidi A* **2004**, 201, 2219.
- [12] E. H. Khan, M. H. Weber, M. D. McCluskey, *Phys. Rev. Lett.* **2013**, 111, 017401.
- [13] J. A. Enterkin, A. K. Subramanian, B. C. Russell, M. R. Castell, K. R. Poeppelmeier, L. D. Marks, *Nat. Mater.* **2010**, 9, 245.
- [14] A. F. Santander-Syro, M. Klein, F. L. Boariu, A. Nuber, P. Lejay, F. Reinert, *Nat. Phys.* **2009**, 5, 637.
- [15] F. A. Selim, M. C. Tarun, D. E. Wall, L. A. Boatner, M. D. McCluskey, *Appl. Phys. Lett.* **2011**, 99, 202109.
- [16] Y. Sato, M. Yodogawa, T. Yamamoto, N. Shibata, Y. Ikuhara, *Appl. Phys. Lett.* **2005**, 86, 152112.
- [17] A. Janotti, C. G. Van de Walle, *Phys. Rev. B* **2007**, 76, 165202.
- [18] S. B. Zhang, A. Zunger, *Appl. Phys. Lett.* **1997**, 71, 677.
- [19] H. Li, L. Geelhaar, H. Riechert, C. Draxl, *Phys. Rev. Lett.* **2015**, 115, 085503.
- [20] T. Yamashita, T. Akiyama, K. Nakamura, T. Ito, *Jpn. J. Appl. Phys.* **2010**, 49, 030212.
- [21] A. Jenichen, C. Engler, B. Rauschenbach, *Surf. Sci.* **2013**, 613, 74.
- [22] C. G. Tang, M. J. S. Spencer, A. S. Barnard, *Phys. Chem. Chem. Phys.* **2014**, 16, 22139.
- [23] I. W. Yeu, J. Park, G. Han, C. S. Hwang, J. H. Choi, *Sci. Rep.* **2017**, 7, 10691.
- [24] K. Reuter, M. Scheffler, *Phys. Rev. B* **2003**, 68, 045407.
- [25] W. X. Li, C. Stampfl, M. Scheffler, *Phys. Rev. B* **2003**, 68, 165412.
- [26] I. W. Yeu, G. Han, J. Park, C. S. Hwang, J. H. Choi, *Sci. Rep.* **2019**, 9, 1127.
- [27] I. W. Yeu, G. Han, J. Park, C. S. Hwang, J. H. Choi, *Appl. Surf. Sci.* **2019**, 497, 143740.
- [28] I. W. Yeu, G. Han, C. S. Hwang, J. H. Choi, *Nanoscale* **2020**, 12, 17703.
- [29] A. Togo, I. Tanaka, *Scr. Mater.* **2015**, 108, 1.